Electrospray-Surface Enhanced Raman Spectroscopy (ES-SERS) for probing surface chemical compositions of atmospherically relevant particles

Masao Gen and Chak K. Chan*

School of Energy and Environment, City University of Hong Kong, Tat Chee Avenue, Kowloon, Hong Kong, China

*E-mail: chak.k.chan@cityu.edu.hk. Phone: +(852)-3442-5593. Fax: +(852)-3442-0688.

Abstract

We present electrospray-surface enhanced Raman spectroscopy (ES-SERS) as a new approach to measuring the surface chemical compositions of atmospherically relevant particles. The surface-sensitive SERS is realized by electrospraying Ag nanoparticle aerosols over analyte particles. Spectral features at $\nu(SO_4^{2-})$, ν(C-H) and ν(O-H) modes were observed from the normal Raman and SERS measurements of laboratory-generated supermicron particles of ammonium sulfate (AS), AS mixed with succinic acid (AS/SA) and AS mixed with sucrose (AS/sucrose). SERS measurements showed strong interaction (or chemisorption) between Ag nanoparticles and surface aqueous sulfate [SO_4^{2-}] with $[SO_4^{2-}]_{AS/sucrose} > [SO_4^{2-}]_{AS/SA} > [SO_4^{2-}]_{AS}$. Enhanced spectra of the solid AS and AS/SA particles revealed the formation of surface-adsorbed water on their surfaces at 60% relative humidity. These observations of surface aqueous sulfate and adsorbed water demonstrate a possible role of surface-adsorbed water in facilitating the dissolution of sulfate from the bulk phase into its water layer(s). Submicron ambient aerosol particles collected in Hong Kong exhibited non-enhanced features of black carbon and enhanced features of sulfate and organic matter (carbonyl group), indicating an enrichment of sulfate and organic matter on the particle surface.

1. Introduction

Atmospheric aerosols are emitted from a variety of sources and complex mixtures of organic and inorganic substances (Ault and Axson, 2017). Due to the complex components, aerosols have a wide range of physical and chemical properties (Hinds, 1999; Sullivan and Prather, 2005; Ault and Axson, 2017). Aerosols affect both the climate and human health on a global scale (IPCC, 2013; Pope and Dockery, 2006). They scatter and absorb solar radiation and alter the properties of clouds, potentially affecting radiative transfer and precipitation behaviors (IPCC, 2013; DeMott et al., 2016). Exposure to particulate matter (PM) has adverse effects on cardiopulmonary health (Pope and Dockery, 2006).

Thin film water is ubiquitous and can cover the surfaces of many materials (Ewing, 2006). Earlier work has reported the formation of a monolayer of adsorbed water on the surface of solid AS at 60% relative humidity (RH) (Romakkaniemi et al., 2001). Surface-adsorbed water plays a potential role in facilitating the heterogeneous chemistry of atmospheric aerosols (Trainic et al., 2012; Chu and Chan, 2016). Yet the relative role of surface chemistry and bulk processes is poorly understood due to the lack of surface-sensitive techniques available for studying individual atmospheric particles (Ault et al., 2013).

Spectroscopic methods, particularly Raman spectroscopy, are useful for investigating the physical properties and chemical components of complex atmospheric particles. Raman studies have been carried out to probe the phase state (Bertram et al., 2011), hygroscopic properties (Yeung et al., 2009), and heterogeneous reactivity (Lee and Chan, 2007) of laboratory-generated atmospherically relevant particles at precisely controlled RHs. However, Raman measurements of atmospherically relevant particles have been limited to the highly Raman-active modes of $\nu(SO_4^{2-})$ (Yeung et al., 2009), $\nu(NO_3^-)$ (Lightstone et al., 2000), ν(C-H) (Chu and Chan, 2016) and black carbon (BC) (Sze et al., 2001), due to insufficient

sensitivity to other modes. In addition, Sobanska et al. (2012) reported a strong fluorescence signal from the humic substances in clay mineral aerosols, which can mask Raman signals (Sobanska et al., 2012). Expanding the detection range of Raman as well as enhancing Raman signals can help elucidate particle phase processes occurring in the atmosphere.

Recently surface enhanced Raman spectroscopy (SERS) and tip enhanced Raman spectroscopy (TERS) have been applied for characterizing atmospheric particles (Craig et al., 2015; Ofner et al., 2016). SERS has the potential to overcome the limitations of insufficient sensitivity and spatial resolution in conventional Raman spectroscopy. The technique relies on the localized surface plasmon resonances in noble metal nanoparticles (e.g. silver and gold) to trigger Raman enhancement (Jeanmaire and Van Duyne, 1977; Albrecht and Creighton, 1977). Raman signals can be enhanced by up to 10^{10} times (Le Ru et al., 2007). Earlier works detected not only the highly Raman-active modes but also other important modes such as *v*(C-C), *v*(C-N), *v*(C=O) and *v*(O-H) modes in atmospheric particles (Craig et al., 2015; Ofner et al., 2016). Craig et al. (2015) made use of SERS substrates coated with silver (Ag) nanoparticles for collection of ambient or analyte particles (Craig et al., 2015). Despite the successful enhancement of Raman signals within individual analyte particles, approaches using SERS substrates may not be able to detect the surface chemical compositions of particles. This limitation is attributable to the configuration of SERS active spots that are formed between the SERS substrate and the analyte particle.

In most microscopic Raman studies, backscattered Raman signals of analyte particles are collected in a microscopic configuration. When the analyte particles are deposited on the Ag-coated SERS substrate (Craig et al., 2015), SERS active spots are located beneath the particles. In other words, the photons must pass through the particle with a refractive index greater than air, which would scatter/absorb light and reduce the signals received by the Raman microscope. Furthermore, the SERS-substrate method collects enhanced Raman signals from

interfaces between the substrate and deposited particles but not the gas/particle interfaces, which are important for heterogeneous processes. A significant enhancement was observed only at the edge of particles likely due to spatially non-uniform SERS active spots distributed across individual particles (Craig et al., 2015).

Gen and Lenggoro (2015) recently developed an SERS approach to probe surfaces coated with an organic thin film by electrospraying Ag nanoparticle aerosols over the probed surfaces (Gen and Lenggoro, 2015). A number concentration of 11.6 particles/μm^2 and a narrow distribution of separation distance between deposited particles peaking at 100 nm confirmed the concentrated and uniform deposition pattern of Ag nanoparticles on a substrate respectively. They employed the electrospray deposition of positively charged Ag nanoparticles on a silicon wafer that had been dip-coated with an organic thin film. The concentration of the organics on the substrate ranged from ~1 to 30 nanograms/m^2. The Raman mapping allows direct measurement of a spatial distribution of organic molecules on a solid surface with the detection limit above 3.54 molecules/μm^2. Numerical electrodynamic simulations have revealed that singly charged Ag nanoparticles (50 nm) can be deposited on any surface, i.e., from metallic to non-metallic substrates, under an electric field of > 10^4 V/m. Following that approach, we devise an SERS technique to detect the surface chemical compositions of deposited analyte particles by creating uniform SERS active spots on the particle surface. Figure 1 shows a comparison of approaches using an SERS substrate with pre-deposited metal nanoparticles and our proposed method of depositing metal nanoparticle aerosols on collected analyte particles. Deposition of metal nanoparticle aerosols on an analyte particle creates SERS active spots on the surface of the analyte particle facing the microscope, similar to the TERS configuration (Uzayisenga et al., 2012; Yang et al., 2009) and therefore the photons from the enhancement can be directly transferred to a detector without passing through the analyte particle.

Aerosol technology has been used to generate aerosols with a wide range of sizes across five orders of magnitude (Hinds, 1999; Okuyama and Lenggoro, 2003; Jaworek, 2007). Among the techniques, the electrospray technique is a unique method that atomizes liquid using electrical forces (de la Mora, 2007). It can produce submicron highly charged droplets, thus preventing their coagulation and facilitating their self-dispersion. After solvent evaporation, dried aerosols form rapidly at ambient temperatures and pressure. Since charges on droplets can remain in dried aerosols, the motion of highly-charged dried aerosols can be precisely controlled using electric fields (Kim et al., 2006; Lenggoro et al., 2006).

We report for the first time a technique called electrospray-SERS (ES-SERS) which is designed to probe atmospherically relevant particles. We employ the electrospray technique to deposit Ag nanoparticles on analyte particles. We present ES-SERS experiments on laboratory-generated supermicron particles of ammonium sulfate (AS), AS mixed with succinic acid (SA) and AS mixed with sucrose (AS/sucrose). The dependence of Raman enhancement at the $\nu(SO_4^{2-})$ mode on surface sulfate anions is discussed. Effects of analyte particle size on Raman signals are investigated with aqueous AS/sucrose particles. We then describe the direct observation of surface adsorbed water on solid AS and AS/SA particles from enhanced Raman signals of ν(O-H) mode. Lastly, we apply the technique to examine submicron ambient particles.

2. Experimental

2.1. Materials and sample preparation

In this study, atmospherically relevant particles of AS, AS mixed with SA, and AS mixed with sucrose were examined (Ling and Chan, 2008; Zobrist et al., 2008; Freedman et al., 2010; Chu and Chan, 2016). AS (Sigma-Aldrich) and sucrose (Affymetrix USB Products) were dissolved

in ultrapure water (18.2 MΩ cm) to prepare an AS/Sucrose stock solution of 5 wt% at 1:1 molar ratio. A 5-wt% aqueous solution of AS only and another of AS and SA (Sigma-Aldrich) mixed at 1:1 weight ratio were also prepared. The prepared solution was atomized to produce droplets using a piezoelectric particle generator (Model 201, Uni-Photon Inc.) and the analyte droplets were deposited on a substrate of silicon wafer (100, N type, Y Mart, Inc.) that had been coated with gold using a sputtering device (Q150T, Quorum Technologies Ltd.). The gold coating was used to mask peaks of Si wafer at 520 and 900-1000 cm^{-1}. Ambient PM was collected on gold-coated Si substrates at the South Gate of the Hong Kong University of Science and Technology using a cascade impactor (Model MPS-4G1, California Measurements Inc.) on the morning of 9 May 2016. Collected particles between 0.05 and 0.15 µm in aerodynamic diameter were used as analyte particles. The samples were kept in a desiccator at < 10% RH prior to use and Raman measurements were taken at the ambient RH of 60%. All chemicals were used as received without further purification.

2.2. SERS agent nanoparticles

Ag nanoparticles were deposited on the analyte particles (Fig. 1b) using the electrospray technique (Gen and Lenggoro, 2015). An aqueous suspension of Ag nanoparticles was prepared by reducing silver nitrate with sodium citrate (Lee and Meisel, 1982). The Ag nanoparticles deposited on the substrate and in the suspension were characterized by scanning electron microscopy (SEM; EVO 10, Carl Zeiss Inc. and JSM-6390, JEOL) and UV-vis spectroscopy (UV-3600, Shimadzu), respectively. Ag nanoparticles suspended in the gas phase produced from the electrospray were characterized with a differential mobility analyzer (DMA; Model 3081A, TSI Inc.) and a condensation particle counter (CPC; Model 3025A, TSI Inc.).

176

177 **2.3. Deposition of Ag nanoparticles**

178 Figure 2 shows the electrospray system consisting of a generation and a deposition
179 chamber. The suspension was diluted with an equal volume of ethanol to reduce the surface
180 tension and to facilitate the evaporation of solvents (Gen and Lenggoro, 2015). The diluted
181 suspension was fed to a stainless-steel capillary tube (SUS304; 32 gauge, Hamilton) which
182 serves as a spray nozzle using a syringe pump (KDS-100, KD Scientific) at a liquid flow rate
183 of 0.2 mL/h. The spray nozzle was inserted to a six-way cross chamber and positively charged
184 at 2.0 - 2.5 kV with a high-voltage module (HV1, S1-5P(A)-L2, Matsusada Precision Inc.).
185 The spray current, which is induced by charged droplets, was measured with an electrometer
186 (Model 6485, Keithley Instruments Inc.). CO_2 gas at a flow rate of ~1 L/min was introduced
187 into the chamber to suppress electric discharge (i.e. to maintain stability of electrospraying)
188 (Zeleny, 1915) and carry Ag nanoparticles from the generation chamber to the deposition one.
189 The spray nozzle and the deposition chamber were electrically separated from the generation
190 chamber. The substrate was set perpendicular to the spray nozzle in the deposition chamber
191 and negatively charged at - 2.0 kV using another high-voltage module (HV2, S1-5N(A)-L2,
192 Matsusada Precision Inc.). Ag nanoparticles were deposited on the substrate at ambient
193 pressure (1 atm) and the spraying time was 1 hour based on earlier work (Gen and Lenggoro,
194 2015). The Ag nanoparticles produced were electrically neutralized with a Kr-85 aerosol
195 neutralizer (Model 3077A, TSI Inc.) before entering the DMA for size distribution
196 measurements. Size classification in the DMA was performed by applying a negative voltage
197 to the center rod of the DMA with a high-voltage supplier (HAR-15R2-L, Matsusada Precision
198 Inc.). The voltage supplier was controlled with a data acquisition system (NI PCIe-6361,
199 National Instruments) through a LabVIEW program using the necessary voltage for a specific

range of particle sizes based on the pressure and temperature of the flow in the DMA (Hinds, 1999; Knutson and Whitby, 1975).

2.4. SERS analysis

Analyte particles with and without Ag nanoparticles were characterized using a Raman spectroscope (Renishaw inVia Raman Microscope). Instrument control was performed with the Renishaw WiRE (Renishaw). Through microscopic observations, analyte particles exceeding 20 µm in diameter were selected for most cases of normal Raman and SERS measurements. A 633 nm (17 mW) laser was used and an integration time of 10 s was applied. The sample was irradiated with the laser through a 50X objective lens (N PLANEPI, NA = 0.75, Leica) and the laser spot size was estimated to be ~1 µm. Spectra from multiple positions on an analyte particle were acquired with a step size of 2 µm. Over 10 Raman spectra of 300-4000 cm^{-1} were obtained for each particle. Raman enhancement was observed for vibration modes of $\nu(SO_4^{2-})$, $\nu(NO_3^-)$, ν(C-H), and ν(O-H) at ~970, ~1034, ~2930 and 3200 ~ 3500 cm^{-1}, respectively. Ambient RH and temperature were 60% and 20-21 ºC, respectively. An enhancement factor is used to quantitatively examine the performance of SERS. This factor can be expressed as $(I_{SERS}/N_{Surf})/(I_{NR}/N_{vol})$, where N_{vol} is the average number of analyte molecules within the scattering volume for normal Raman experiments; N_{Surf} is the average number of analyte molecules physically and/or chemically adsorbed on a nanoparticle surface within the scattering volume for SERS experiments; I_{NR} and I_{SERS} are Raman intensities for normal Raman and SERS measurements, respectively (Le Ru et al., 2007). In the current study, we simply used I_{SERS}/I_{NR} for comparing experimental results later because it is difficult to calculate N_{vol}/N_{Surf}.

3. Results and discussion

We first characterize the electrospray technique. Next, SERS measurements of supermicron (1-40 μm) AS, AS/SA and AS/sucrose particles are reported. The presence of surface-adsorbed water is then discussed. Finally, ES-SERS is used to characterize submicron ambient PM. The SERS experimental results are shown in Table 1. More than 10 spectra for normal Raman and SERS measurements were quantified to estimate I_{SERS}/I_{NR}. All spectra for quantification of I_{SERS}/I_{NR} (except for AS /sucrose particles smaller than 20 μm) are shown in Figs. S1, S2 and S3.

3.1. Characterization of the electrospray system

The stability of the electrospraying system was characterized using the current (I)–voltage (V) curve (Figure S4 in the Supporting Information). Stable electrospraying can be obtained within a certain range of V where I does not change (de la Mora and Loscertales, 1994; Lenggoro et al., 2000). In Figure S4, I increases with V at lower V's (<2.0 kV). As V approaches 1.9 kV, I starts to level off and stays almost constant until V reaches 2.3 kV. In the present study, V ranged between 1.9 to 2.3 kV was used for electrospraying.

The dispersion of SERS nanoparticles and their interaction with analyte molecules determine the enhancement behavior (Ko et al., 2008; Oh et al., 2009; Addison and Brolo, 2006; Makiabadi et al., 2010; Sun et al., 2011). Therefore, Ag nanoparticles in the suspension, in the gas phase and deposited on the substrate were characterized. Figure S5 presents the absorption spectra of Ag nanoparticles in the suspension as prepared and as diluted with ethanol at a 1:1 volume ratio. The aqueous suspensions exhibited maximum absorption at ~ 400 nm as a result of the localized surface plasmon resonance, whereas the suspension diluted with

ethanol showed a slight shift to ~420 nm. This insignificant change in the absorption spectrum suggests that the size distribution of Ag nanoparticles is similar before and after dilution. Figure S6 shows the gas-phase size distribution of Ag nanoparticle aerosols with a mode of 53 nm in electrical mobility diameter. The nanoparticles dried from the original suspension and those deposited (electrosprayed) on the gold-coated silicon substrate were observed with SEM as shown in Fig. S7 a and c, respectively. The size distribution of the deposited particles (Fig. S7 d) shows a peak of ~67 nm which is close to the primary particle size (56 nm in Fig. S7 b) and the particle size (53 nm in Fig. S6) of the aerosol from the electrospray. The size of Ag nanoparticles in suspension has been reported to be ~ 50 nm (Gen and Lenggoro, 2015). The similarity in size between particles in the suspension, particles in the gas phase and particles deposited on the substrate gives us confidence that the Ag nanoparticles produced in the current system can be delivered from the suspension onto the substrate surface without much aggregation.

3.2. SERS of laboratory-generated PM

Normal and enhanced Raman spectra of the AS/sucrose particles are shown in Fig. 3. Normal Raman measurement of an AS/sucrose particle (without Ag nanoparticles) shows SO_4^{2-} vibration modes at 450, 633, and 979 cm^{-1} and NH_4^+ vibration modes at 1461, 1700 and 3153 cm^{-1} (Dong et al., 2007). A broad band ν(O-H) of water at ~3400 cm^{-1} can also be seen, indicating that the particle contained bulk water at ambient RH (i.e. 60%). The addition of sucrose delays efflorescence of the mixed particle (Chu and Chan, 2016). Bands ν(C-O) of sucrose at 1067 and 1130 cm^{-1} and a broad band ν(C-H) at 2930 cm^{-1} were also observed (Brizuela et al., 2014). In the presence of Ag nanoparticles, a significant Raman enhancement was found at the $\nu(SO_4^{2-})$ mode of 967 cm^{-1} with I_{SERS}/I_{NR} = 12.4. The I_{SERS}/I_{NR} at $\nu(SO_4^{2-})$

mode is approximately 7.6 times higher than that at ν(C-H) mode (Table 1). This is likely due to the strong interaction between sulfate and Ag nanoparticles. Furthermore, a redshift from 980 to 967 cm^{-1} occurred. A commercially available Ag-coated SERS substrate (SERStrate, Silmeco) (Schmidt et al., 2012) was also used to investigate the Raman enhancement of the AS/sucrose particles (Fig. 4). Likewise, the selective enhancement and the redshift at the $\nu(SO_4^{2-})$ mode were observed. In addition, the spectrum obtained with the SERS substrate (green) is almost identical to the current SERS spectrum (red), giving us confidence that the enhancement observed in the present study was triggered by the deposition of Ag nanoparticle aerosols.

The electrospray system has been proven to be effective in depositing nanoparticles onto any surface (Gen and Lenggoro, 2015). We believe that Ag nanoparticles are deposited onto the analyte particle surfaces because Raman enhancement was observed only when electrospraying Ag nanoparticles was performed. Ag nanoparticles used in the current study were synthesized by the citrate-reduction method. If the nanoparticles were aggregated, SERS spectrum would show enhanced peaks of citrate adsorbed on Ag nanoparticle surface as stabilizer (Munro et al., 1995). In our measurements of AS particles, we observed strong citrate peaks only for one particle (Figure S1(e)), but absent for all other SERS spectra. This gives us confidence that the enhancement is mainly coming from individual Ag nanoparticles.

Strong charge-transfer interaction (i.e. chemisorption) between Ag nanoparticles and analyte molecules generally leads to a peak shift and peak broadening (Campion and Kambhampati, 1998; Stöckle et al., 2000). The strength of coupling is strongly dependent on the orientation and binding of analyte molecules to a nanoparticle surface. Earlier work has suggested that nitrate anions in aqueous form are chemisorbed on Ag nanoparticle surfaces, resulting in a significant enhancement and a redshift of the $\nu(NO_3^-)$ peak (Craig et al., 2015). Similarly, aqueous sulfate is also expected to be chemisorbed on Ag nanoparticles, leading to

a significant enhancement of the $\nu(SO_4^{2-})$ peak. In other words, the availability of aqueous sulfate on the surface of analyte particles, $[SO_4^{2-}]$ could be characterized by the enhancement. To study the Raman enhancement of $[SO_4^{2-}]$, SERS was performed on the AS and AS/SA particles. The sample particles were first dried at below 10% RH and then exposed to 60% RH during the normal Raman and SERS measurements. Both types of particles are in solid form at 60% RH (Laskina et al., 2015; Choi and Chan, 2002). There is no difference in the full width at half maximum (FWHM) and the peak position between AS and AS/SA particles (see Table 2), confirming that the presence of SA does not affect the phase state of AS at 60% RH. Figure 5 shows the normal and SERS spectra of the AS and AS/SA particles. No Raman enhancement at the $\nu(SO_4^{2-})$ mode was observed for the AS particles (i.e. $I_{SERS}/I_{NR} \sim 1$). Since the AS particles were solid during SERS measurements, a negligible amount of aqueous sulfate anions were available. In contrast, the AS/SA particles show an enhancement at δ(OH···O), $\nu(SO_4^{2-})$ and ν(C-H) modes with the I_{SERS}/I_{NR} of 3.7, 3.3 and 2.6, respectively. The I_{SERS}/I_{NR} at the $\nu(SO_4^{2-})$ mode is significantly smaller than I_{SERS}/I_{NR} = 12.4 for the AS/sucrose particles, suggesting that less surface aqueous sulfate for the AS/SA particles was available than that for the AS/sucrose particles. SA, which is only slightly soluble in water, crystallizes and forms nuclei during the partial efflorescence of ammonium nitrate and AS (Lightstone et al., 2000). The presence of SA does not affect the deliquescence behavior of AS (Choi and Chan, 2002). Nonetheless, the current results clearly demonstrate that the addition of SA into AS has a substantial influence on the availability of aqueous sulfate anions on the analyte particle surface but not so much on their availability in the AS particle system. Overall, SERS experiments reveal the availability of surface aqueous sulfate in the three particle systems: $[SO_4^{2-}]_{AS/sucrose}$ (I_{SERS}/I_{NR} = 12.4) > $[SO_4^{2-}]_{AS/SA}$ (I_{SERS}/I_{NR} = 3.3) > $[SO_4^{2-}]_{AS}$ (I_{SERS}/I_{NR} = 1).

Particle phase can be inferred from the position and shape of the Raman peaks (Yeung and Chan, 2010). Table 2 shows the peak position and FWHM of the $\nu(SO_4^{2-})$ mode obtained

using Gaussian fittings. When AS deliquesces, the $\nu(SO_4^{2-})$ peak is generally blue-shifted and broadened. In the normal Raman measurements, AS and AS/SA particles show a sharp peak at 977 cm^{-1} with FWHM of <8 cm^{-1} but the AS/sucrose particles show a peak at 980 cm^{-1} with FWHM of 13.5 cm^{-1}. The blueshift and band broadening strongly suggest the presence of aqueous sulfate in the AS/sucrose particles, whereas the other particles contain sulfate in solid form. In the SERS measurements, however, the redshift and increase in FWHM are most likely due to strong interaction between Ag nanoparticles and surface aqueous sulfate (Niaura and Malinauskas, 1998). The shape of the $\nu(SO_4^{2-})$ peak for the AS particles did not change between the two measurements, indicating no or weak interaction between Ag nanoparticles and sulfate in solid form.

Figure 6 shows Raman intensities at the $\nu(SO_4^{2-})$ mode along the diameter of individual AS/sucrose particles from normal Raman and SERS measurements. The laser spot transected the particle surface from one edge to another edge with a step size of 2 μm. Normal Raman measurement showed peaks of the $\nu(SO_4^{2-})$ mode at all positions. SERS measurement showed an enhancement at all positions, although the Raman intensity fluctuated. The results demonstrate the high-frequency Raman enhancement across an individual particle. The higher SERS intensities near the edges might be due to the higher densities of SERS active spots in the sensing volume of the laser spot.

3.3. Size effect on Raman intensity

One of the essential requirements for Raman enhancement is that analyte molecules must be located within a few nanometers of the nanoparticle surface (Dieringer et al., 2006). Raman emissions from analyte molecules far from the surface cannot be enhanced. Hence, the enhanced Raman spectra can provide chemical information about the surface of analyte

particles. Here we examine the effect of analyte particle size (i.e. particle volume) on Raman signals to confirm the surface-sensitive Raman emissions. Figure 7 shows the typical normal Raman spectrum of AS/sucrose particles and the intensities of $\nu(SO_4^{2-})$ and ν(C-H) as a function of the particle size. Small particles were produced using stock solutions of AS/sucrose diluted by a factor of 10 and 100. Above 10 µm in particle size, the Raman intensity stays almost constant for both modes. When the particle size is below 10 µm, the Raman intensity decreases with particle size. Raman intensity is correlated with the number of analyte molecules in the sensing volume of the focused laser spot. The size dependence indicates that normal Raman measurements are sensitive to the particle volume and provides bulk information about the chemical composition of analyte particles. Note that the laser spot size is smaller than any of the particle size studied and therefore particle width has no effect on the intensity. However, the depth of focus, *h*, contributes to the size effect on the intensity. If the analyte particle depth is comparable to or smaller than *h*, the Raman intensity decreases with the number of molecules within the sensing volume. The estimated *h* in our experiments is 2.3 µm using $h = 2\lambda/NA^2$ where λ (633 nm) and *NA* (0.75) are the wavelength of the laser and the numerical aperture of the objective lens, respectively. This estimated value is smaller than the nominal threshold of 10 µm observed in the size dependence of the normal Raman signals, because gravity had affected the shape of the analyte particles deposited on the substrate, reducing the particle height (<10 µm). Gravity deforms the shape of droplets on a substrate, when the size of droplet is sufficiently large (e.g. > 10 µm). A contact angle of large droplet to a substrate is much smaller than 180 degrees. Thus, the depth of substrate-deposited droplet is typically smaller than its diameter. Earlier work using environmental SEM has shown that AS droplets are hemispherical when in contact at 96° with a copper substrate that has been hydrophobically modified with poly-tetrafluoroethylene (Matsumura and Hayashi, 2007).

Figure 8 shows the typical enhanced spectra of the AS/sucrose and the intensity as a function of particle size for the two modes. Unlike the normal Raman measurements, the enhanced intensity as a function of particle size was almost constant. SERS active spots were created over the surface of analyte particles and the surface area irradiated by a laser was constant over the size range studied due to the smaller laser spot diameter. Furthermore, in the normal Raman measurements, a change in particle size changes the Raman intensity when the particle volume is comparable to the sensing volume of the laser spot. Considering these facts, the constant enhanced intensity provides evidence that the enhanced spectrum contains information about the bulk chemical compositions (non-enhanced component) as well as the surface compositions (enhanced component), making the ES-SERS technique suitable for surface-sensitive detection.

The I_{SERS}/I_{NR} ratio as a function of particle size for the AS/sucrose particles is summarized in Table 1. I_{SERS} was calculated by averaging enhanced peak intensities from all SERS measurements (the entire size range). The normal Raman intensity decreases with size below 10 µm. Hence I_{SERS}/I_{NR} increases with decreasing size, resulting in the largest I_{SERS}/I_{NR} of 162.0 for the $\nu(SO_4^{2-})$ mode at a particle size of 1.4 µm. Craig et al. (2015) reported an enhancement factor of 2.0 at $\nu(SO_4^{2-})$ mode of ~970 cm^{-1} using an SERS substrate with the AS particles on the top of Ag nanoparticles on the substrate. Furthermore, Fu et al. (2017) reported an enhancement factor of 6.1 for the same mode, using commercial SERS substrates with pre-determined gold-coated structure of inverted pyramids (Klarite, Renishaw Diagnostics Ltd.). Our results of AS/sucrose particles (Table 1) showed that the I_{SERS}/I_{NR}, which is the lower limit of enhancement factor, ranged from 12.4 to 163, much higher than the above studies. Note that I_{SERS}/I_{NR} is the lower limit of the enhancement factor ($I_{SERS}N_{vol}/I_{NR}N_{surf}$) conventionally used because N_{vol}/N_{Surf} is much greater than unity in the present case.

3.4. Measurements of surface-adsorbed water

Taking advantage of the surface sensitiveness of ES-SERS, we examine the presence of surface-adsorbed water on solid particles of AS and AS/SA. As shown in Fig. 3 and Table 2, AS/sucrose particles (1:1 molar ratio) at 60% RH are aqueous, which can be inferred from the blueshift in the $\nu(SO_4^{2-})$ peak compared to the AS particles, a broad peak at the ν(C-H) mode and the appearance of the ν(O-H) mode of water (~3400 cm^{-1}). The enhancement at the ν(O-H) mode (I_{SERS}/I_{NR} = 1.2) was observed in the AS/sucrose particles, but bulk water might have contributed to the enhancement. Figure 9 presents the normal and enhanced Raman spectra of solid AS and AS/SA particles at 3000 ~ 4000 cm^{-1} at 60% RH, and reveals a possible role of surface-adsorbed water formed on the particles. No water peak was observed at ν(O-H) in the normal Raman measurements of either particle system (blue spectra) confirming that the particle phases were likely solid and the bulk water in the particles was negligible (undetectable). In contrast, the SERS experiments presented a slightly enhanced water peak for the AS particles and a significant enhancement for the AS/SA particles. The thickness of surface-adsorbed water on AS at 60% has been reported to be ~ 0.19 nm (a monolayer) (Romakkaniemi et al., 2001). The slight enhancement reflects the detection limit in our approach (i.e. a water film of monolayer thickness). The significant enhancement for AS/SA particles, which was much larger than that for AS particles, suggests that they had more than one layer of adsorbed water at 60% RH. The presence of water at 60% RH could explain the gradual mass increase of AS/SA particles before abrupt water uptake at deliquescence (Ling and Chan, 2008). The relative mass change (m/m_0) obtained with an electrodynamic balance increases with RH: m/m_0 = 1.0, 1.2, 1.3 and 2.0 at 50%, 80%, 81% and 82% RH, respectively. Corresponding Raman spectra did not show a distinct peak at ν(O-H) mode at RHs between 50 and 81%.

The surface-adsorbed water may have facilitated the dissolution of sulfate anions into its layer(s) from the bulk particle, thus contributing to an increase in aqueous sulfate anions on the surface (Fig. 9c). In other words, the surface-adsorbed water is likely associated with the aqueous sulfate anions on the surface, which is consistent with our observation on the availability of aqueous sulfate anions for the AS and AS/SA particles ($[SO_4^{2-}]_{AS/SA} > [SO_4^{2-}]_{AS}$). Sulfate in the bulk solid phase dissolved in the surface-adsorbed water layer(s) and was subsequently chemisorbed on the surface of an Ag nanoparticle, leading to a significant Raman enhancement and a peak shift.

3.5. Ambient PM

Lastly, we present SERS experiments of ambient PM. Figure 10 shows the normal and enhanced Raman spectra of the ambient PM and the conceptual representations of the analyte particles for normal Raman and SERS measurements. The normal spectrum has peak bands of SO_4^{2-} vibration at 451, 615 and 977 cm^{-1} as well as disorder (D) and graphite (G) peak bands at 1341 and 1598 cm^{-1} respectively. The presence of D and G bands reveals that the particles contain non-graphite and graphite components, which are often referred to as amorphous carbon or black carbon (BC) (Sze et al., 2001). The SERS experiments show a small enhancement at bands of 963 cm^{-1} (I_{SERS}/I_{NR} = 1.9) for sulfate and 1039 cm^{-1} (I_{SERS}/I_{NR} = 1.6) for nitrate, but no enhancement of the D and G peaks. I_{SERS}/I_{NR} was quantified from the measurements from 43 different positions on the substrate. A water peak band was not found at ~3400 cm^{-1} (not shown), suggesting that the bulk water was negligible. Nonetheless, the small enhancement at 963 cm^{-1} indicates the presence of surface-adsorbed water on ambient PM at 60% RH, which helps sulfate dissolve in the water layer(s). A peak shift from 977 to 963 cm^{-1} and an increase in FWHM from 7.6 to 26.0 cm^{-1} indicate that sulfate anions were

chemisorbed on the Ag particle surface (Fig. 9c). Additionally, the enhanced spectrum presents a peak band at 1777 cm^{-1}, which can be assigned to the carbonyl group. A similar observation using normal Raman spectroscopy has been reported for particles collected in Hamilton, Ontario (Sze et al., 2001). The PM probably contained organics, but the amount of organics could not be detected in mass in the normal Raman measurements. Overall, the normal Raman spectra represent the bulk chemical compositions of BC and sulfate. The enhanced spectra exhibit the bulk chemical compositions together with the surface compositions (e.g. sulfate and the carbonyl group). On the basis of the selective enhancement of the sulfate peak and to a lesser extent the carbonyl peak, we postulate that these BC particles may have been coated with organics and sulfate. In the atmosphere, BC aerosols are usually internally mixed with organics and sulfate after aging (Shiraiwa et al., 2007). An integrated approach using Raman spectroscopy and sum frequency generation spectroscopy has shown that organic material primarily exists at the gas/particle interface of sea spray aerosols (Ault et al., 2013). The spectrum obtained from ES-SERS contains both bulk and surface information of chemical compositions, but only the surface compositions are enhanced due to the distance-dependence effect (Dieringer et al., 2006). The complementary methods of Raman spectroscopy and ES-SERS (as surface-sensitive spectroscopy) can provide the bulk and surface chemical compositions, respectively by comparing normal and enhanced Raman spectra. They potentially help reveal the internal structure of individual particles such as their core/shell structure.

4. Conclusions

We demonstrated a new technique called ES-SERS for probing atmospherically relevant particle compositions. ES-SERS measurements showed that the I_{SERS}/I_{NR} ratios of the $\nu(SO_4^{2-})$

474 band at ~970 cm^{-1} for laboratory-generated AS, AS/SA and AS/sucrose particles followed the
475 order: AS/sucrose (I_{SERS}/I_{NR} = 12.4) > AS/SA (I_{SERS}/I_{NR} = 3.3) > AS (I_{SERS}/I_{NR} = 1). I_{SERS}/I_{NR}
476 is likely associated with the availability of aqueous sulfate anions on the surface, which can be
477 characterized by the enhanced Raman signals, the redshift and the increase in FWHM due to
478 the chemisorption of aqueous sulfate anions on Ag nanoparticles.

479 The ES-SERS technique also allows us to probe the presence of surface-adsorbed water.
480 At 60% RH, the normal Raman spectra of solid AS and AS/SA particles do not exhibit a peak
481 band of ν(O-H) at ~3400 cm^{-1} but the enhanced spectra show a small enhancement for AS
482 particles and a significant enhancement for AS/SA particles. The latter is attributable to water
483 adsorbed on the surface of the solid particles. The surface-adsorbed water may promote the
484 dissolution of sulfate from the bulk phase into its water layer(s). The enhanced $\nu(SO_4^{2-})$ peaks
485 also revealed that the AS/SA particles have more surface aqueous sulfate than do the AS
486 particles.

487 While the normal Raman intensity was sensitive to the particle size, the enhanced
488 Raman intensity was insensitive in the size range studied (1 ~ 40 μm). In fact, the enhanced
489 intensity was constant over the entire size range. Increasing attention has been paid to
490 spectroscopic analysis which can provide valuable information on the physicochemical
491 properties of atmospheric particles at the single-particle level (Ciobanu et al., 2009; Baustian
492 et al., 2012; Yeung et al., 2009). One of the biggest limitations is that particles must be at least
493 1 μm in size for particle analysis to be possible due to the Abbe diffraction limit. Our ES-SERS
494 results demonstrate that the enhanced Raman signals do not drop as the particle size decreases
495 down to 2 μm. The high sensitivity is likely due to the configuration of the SERS active spots.
496 This sensitive technique may be extended to submicron particles in future studies.

497 Normal spectra of ambient submicron PM show the D and G bands and the $\nu(SO_4^{2-})$
498 band, revealing that the particles contain amorphous carbon (i.e. BC) and sulfate. The enhanced

spectra exhibit selective enhancement of $\nu(SO_4^{2-})$ and ν(C=O) modes but no enhancement for the D and G bands. Based on a comparison of the spectra, we postulate a particle morphology with sulfate and organics surrounding the BC core.

The direct contact of Ag nanoparticles to analyte molecules results in a peak shift, which could pose an obstacle to tracing the phase transition as well as identifying functional groups. Recent studies have introduced the use of core-shell composite gold nanoparticles to eliminate the chemical enhancement (Li et al., 2010; Li et al., 2013). The outermost inert shell layer of the nanoparticle prevents its direct contact (i.e. coupling) with analyte molecules. Using such novel nanoparticles could further extend the application of the proposed ES-SERS technique in atmospheric studies.

Acknowledgements

The authors would like to acknowledge Prof. Chun Sing Lee and Dr. Zhi Ning of City University of Hong Kong for the use of their Raman spectrometer and condensation particle counter respectively. The authors also would like to acknowledge Hong Kong University of Science and Technology for the use of their scanning electron microscope (JSM-6390, JEOL).

References

Addison, C. J., and Brolo, A. G.: Nanoparticle-containing structures as a substrate for surface-enhanced Raman scattering, Langmuir, 22, 8696-8702, doi: 10.1021/la061598c, 2006.

Albrecht, M. G., and Creighton, J. A.: Anomalously intense Raman-spectra of pyridine at a silver electrode, J. Am. Chem. Soc., 99, 5215-5217, doi: 10.1021/ja00457a071, 1977.

Ault, A. P., and Axson, J. L.: Atmospheric aerosol chemistry: spectroscopic and microscopic advances, Anal. Chem., 89, 430-452, doi: 10.1021/acs.analchem.6b04670, 2017.

Ault, A. P., Zhao, D., Ebben, C. J., Tauber, M. J., Geiger, F. M., Prather, K. A., and Grassian, V. H.: Raman microspectroscopy and vibrational sum frequency generation spectroscopy as probes of the bulk and surface compositions of size-resolved sea spray aerosol particles, Phys. Chem. Chem. Phys., 15, 6206-6214, doi: 10.1039/c3cp43899f, 2013.

Baustian, K. J., Cziczo, D. J., Wise, M. E., Pratt, K. A., Kulkarni, G., Hallar, A. G., and Tolbert, M. A.: Importance of aerosol composition, mixing state, and morphology for

heterogeneous ice nucleation: A combined field and laboratory approach, J. Geophys. Res., 117, D06217, doi: 10.1029/2011jd016784, 2012.

Bertram, A. K., Martin, S. T., Hanna, S. J., Smith, M. L., Bodsworth, A., Chen, Q., Kuwata, M., Liu, A., You, Y., and Zorn, S. R.: Predicting the relative humidities of liquid-liquid phase separation, efflorescence, and deliquescence of mixed particles of ammonium sulfate, organic material, and water using the organic-to-sulfate mass ratio of the particle and the oxygen-to-carbon elemental ratio of the organic component, Atmos. Chem. Phys., 11, 10995-11006, doi: 10.5194/acp-11-10995-2011, 2011.

Brizuela, A. B., Castillo, M. V., Raschi, A. B., Davies, L., Romano, E., and Brandán, S. A.: A complete assignment of the vibrational spectra of sucrose in aqueous medium based on the SQM methodology and SCRF calculations, Carbohydr. Res., 388, 112-124, doi: 10.1016/j.carres.2013.12.011, 2014.

Campion, A., and Kambhampati, P.: Surface-enhanced Raman scattering, Chem. Soc. Rev., 27, 241-250, doi: 10.1039/a827241z, 1998.

Choi, M. Y., and Chan, C. K.: The effects of organic species on the hygroscopic behaviors of inorganic aerosols, Environ. Sci. Technol., 36, 2422-2428, doi: 10.1021/es0113293, 2002.

Chu, Y., and Chan, C. K.: Reactive uptake of dimethylamine by ammonium sulfate and ammonium sulfate–sucrose mixed particles, J. Phys. Chem. A, 121, 206–215, doi: 10.1021/acs.jpca.6b10692, 2016.

Ciobanu, V. G., Marcolli, C., Krieger, U. K., Weers, U., and Peter, T.: Liquid-liquid phase separation in mixed organic/inorganic aerosol particles, J. Phys. Chem. A, 113, 10966-10978, doi: 10.1021/jp905054d, 2009.

Craig, R. L., Bondy, A. L., and Ault, A. P.: Surface enhanced Raman spectroscopy enables observations of previously undetectable secondary organic aerosol components at the

individual particle level, Anal. Chem., 87, 7510-7514, doi: 10.1021/acs.analchem.5b01507, 2015.

de la Mora, J. F.: The fluid dynamics of Taylor cones, Annu. Rev. Fluid Mech., 39, 217-243, doi: 10.1146/annurev.fluid.39.050905.110159, 2007.

de la Mora, J. F., and Loscertales, I. G.: The current emitted by highly conducting Taylor cones, J. Fluid Mech., 260, 155-184, doi: 10.1017/s0022112094003472, 1994.

DeMott, P. J., Hill, T. C. J., McCluskey, C. S., Prather, K. A., Collins, D. B., Sullivan, R. C., Ruppel, M. J., Mason, R. H., Irish, V. E., Lee, T., Hwang, C. Y., Rhee, T. S., Snider, J. R., McMeeking, G. R., Dhaniyala, S., Lewis, E. R., Wentzell, J. J. B., Abbatt, J., Lee, C., Sultana, C. M., Ault, A. P., Axson, J. L., Martinez, M. D., Venero, I., Santos-Figueroa, G., Stokes, M. D., Deane, G. B., Mayol-Bracero, O. L., Grassian, V. H., Bertram, T. H., Bertram, A. K., Moffett, B. F., and Franc, G. D.: Sea spray aerosol as a unique source of ice nucleating particles, Proc. Natl. Acad. Sci. U.S.A., 113, 5797-5803, doi: 10.1073/pnas.1514034112, 2016.

Dieringer, J. A, McFarland, A. D., Shah, N. C., Stuart, D. A., Whitney, A. V., Yonzon, C. R., Young, M. A., Zhang, X., and Van Duyne, R. P.: Surface enhanced Raman spectroscopy: new materials, concepts, characterization tools, and applications, Farad. Discuss., 132, 9-26, doi: 10.1039/B513431P, 2006.

Dong, J. L., Li, X. H., Zhao, L. J., Xiao, H. S., Wang, F., Guo, X., and Zhang, Y. H.: Raman observation of the interactions between NH_4^+, SO_4^{2-}, and H_2O in supersaturated $(NH_4)_2SO_4$ droplets, J. Phys. Chem. B, 111, 12170-12176, doi: 10.1021/jp072772o, 2007.

Ewing, G. E.: Ambient thin film water on insulator surfaces, Chem. Rev., 106, 1511-1526, doi: 10.1021/cr040369x, 2006.

598 Freedman, M. A., Baustian, K. J., Wise, M. E., and Tolbert, M. A.: Characterizing the
599 morphology of organic aerosols at ambient temperature and pressure. Anal. Chem., 82,
600 7965-7972, doi: 10.1021/ac101437w, 2010.
601 Fu, Y., Kuppe, C., Valev, V. K., Fu, H., Zhang, L., and Chen, J.: Surface-enhanced Raman
602 spectroscopy: A facile and rapid method for the chemical component study of
603 individual atmospheric aerosol, Environ. Sci. Technol, 51, 6260-6267, doi:
604 10.1021/acs.est.6b05910, 2017.
605 Gen, M., and Lenggoro, I. W.: Probing a dip-coated layer of organic molecules by an aerosol
606 nanoparticle sensor with sub-100 nm resolution based on surface-enhanced Raman
607 scattering, RSC Adv., 5, 5158-5163, doi: 10.1039/c4ra03850a, 2015.
608 Hinds, W. C.: Aerosol Technology: Properties, Behavior, and Measurement of Airborne
609 Particles, New York, Wiley, 1999.
610 IPCC: Climate Change 2013: The Physical Science Basis: Summary for Policymakers,
611 Cambridge, UK, 2013.
612 Jaworek, A.: Micro- and nanoparticle production by electrospraying, Powder Technol., 176,
613 18-35, doi: 10.1016/j.powtec.2007.01.035, 2007.
614 Jeanmaire, D. L., and Van Duyne, R. P.: Surface raman spectroelectrochemistry: Part I.
615 Heterocyclic, aromatic, and aliphatic amines adsorbed on the anodized silver electrode,
616 J. Electroanal. Chem., 84, 1-20, doi: 10.1016/s0022-0728(77)80224-6, 1977.
617 Kim, H., Kim, J., Yang, H., Suh, J., Kim, T., Han, B., Kim, S., Kim, D. S., Pikhitsa, P. V., and
618 Choi, M.: Parallel patterning of nanoparticles via electrodynamic focusing of charged
619 aerosols, Nat. Nanotechnol., 1, 117-121, doi: 10.1038/nnano.2006.94, 2006.
620 Knutson, E. O., and Whitby, K. T.: Aerosol classification by electric mobility: apparatus,
621 theory, and applications, J. Aerosol Sci., 6, 443-451, doi: 10.1016/0021-8502(75)
622 90060-9, 1975.

623 Ko, H., Singamaneni, S., and Tsukruk, V. V.: Nanostructured surfaces and assemblies as SERS
624 media, Small, 4, 1576-1599, doi: 10.1002/smll.200800337, 2008.
625 Laskina, O., Morris, H. S., Grandquist, J. R., Qiu, Z., Stone, E. A., Tivanski, A. V., and
626 Grassian, V. H.: Size matters in the water uptake and hygroscopic growth of
627 atmospherically relevant multicomponent aerosol particles, J. Phys. Chem. A, 119,
628 4489-4497, doi: 10.1021/jp510268p, 2015.
629 Le Ru, E. C., Blackie, E., Meyer, M., and Etchegoin, P. G.: Surface enhanced Raman scattering
630 enhancement factors: A comprehensive study, J. Phys. Chem. C, 111, 13794-13803,
631 doi: 10.1021/jp0687908, 2007.
632 Lee, A. K. Y., and Chan, C. K.: Heterogeneous reactions of linoleic acid and linolenic acid
633 particles with ozone: Reaction pathways and changes in particle mass, hygroscopicity,
634 and morphology, J. Phys. Chem. A, 111, 6285-6295, doi: 10.1021/jp071812l, 2007.
635 Lee, P. C., and Meisel, D.: Adsorption and surface-enhanced Raman of dyes on silver and gold
636 sols, J. Phys. Chem., 86, 3391-3395, doi: 10.1021/j100214a025, 1982.
637 Lenggoro, I. W., Lee, H. M., and Okuyama, K.: Nanoparticle assembly on patterned
638 "plus/minus" surfaces from electrospray of colloidal dispersion, J. Colloid Interface
639 Sci., 303, 124-130, doi: 10.1016/j.jcis.2006.07.033, 2006.
640 Lenggoro, I. W., Okuyama, K., de la Mora, J. F., and Tohge, N.: Preparation of ZnS
641 nanoparticles by electrospray pyrolysis, J. Aerosol Sci., 31, 121-136, doi:
642 10.1016/s0021-8502(99)00534-0, 2000.
643 Li, J. F., Huang, Y. F., Ding, Y., Yang, Z. L., Li, S. B., Zhou, X. S., Fan, F. R., Zhang, W.,
644 Zhou, Z. Y., Wu, D. Y., Ren, B., Wang, Z. L., and Tian, Z. Q.: Shell-isolated
645 nanoparticle-enhanced Raman spectroscopy, Nature, 464, 392-395, doi:
646 10.1038/nature08907, 2010.

Li, J. F., Tian, X. D., Li, S. B., Anema, J. R., Yang, Z. L., Ding, Y., Wu, Y. F., Zeng, Y. M., Chen, Q. Z., Ren, B., Wang, Z. L., and Tian, Z. Q.: Surface analysis using shell-isolated nanoparticle-enhanced Raman spectroscopy, Nat. Protoc., 8, 52-65, doi: 10.1038/nprot.2012.141, 2013.

Lightstone, J. M., Onasch, T. B., Imre, D., and Oatis, S.: Deliquescence, efflorescence, and water activity in ammonium nitrate and mixed ammonium nitrate/succinic acid microparticles, J. Phys. Chem. A, 104, 9337-9346, doi: 10.1021/jp002137h, 2000.

Ling, T. Y., and Chan, C. K.: Partial crystallization and deliquescence of particles containing ammonium sulfate and dicarboxylic acids, J. Geophys. Res., 113, D14205, doi: 10.1029/2008jd009779, 2008.

Makiabadi, T., Bouvrée, A., Le Nader, V., Terrisse, H., and Louarn, G.: Preparation, optimization, and characterization of SERS sensor substrates based on two-dimensional structures of gold colloid, Plasmonics, 5, 21-29, doi: 10.1007/s11468-009-9110-6, 2010.

Matsumura, T., and Hayashi, M.: Hygroscopic growth of an $(NH_4)_2SO_4$ aqueous solution droplet measured using an environmental scanning electron microscope (ESEM), Aerosol Sci. Technol., 41, 770-774, doi: 10.1080/02786820701436831, 2007.

Munro, C. H., Smith, W. E., Garner, M., Clarkson, J. W. P. C., and White, P. C.: Characterization of the surface of a citrate-reduced colloid optimized for use as a substrate for surface-enhanced resonance Raman scattering, Langmuir, 11, 3712-3720, doi: 10.1021/la00010a021, 1995.

Niaura, G., and Malinauskas, A.: Surface-enhanced Raman spectroscopy of ClO_4^- and SO_4^{2-} anions adsorbed at a Cu electrode, J. Chem. Soc. Faraday Trans., 94, 2205-2211, doi: 10.1039/a800574e, 1998.

Ofner, J., Deckert-Gaudig, T., Kamilli, K. A., Held, A., Lohninger, H., Deckert, V., and Lendl, B.: Tip-enhanced Raman spectroscopy of atmospherically relevant aerosol nanoparticles, Anal. Chem., 88, 9766-9772, doi: 10.1021/acs.analchem.6b02760, 2016.

Oh, M. K., Yun, S., Kim, S. K., and Park, S.: Effect of layer structures of gold nanoparticle films on surface enhanced Raman scattering, Anal. Chim. Acta, 649, 111-116, doi: 10.1016/j.aca.2009.07.025, 2009.

Okuyama, K., and Lenggoro, I. W.: Preparation of nanoparticles via spray route, Chem. Eng. Sci., 58, 537-547, doi: 10.1016/s0009-2509(02)00578-x, 2003.

Pope, C. A., and Dockery, D. W.: Health effects of fine particulate air pollution: Lines that connect, J. Air & Waste Manage. Assoc., 56, 709-742, doi: 10.1080/10473289.2006.10464485, 2006.

Romakkaniemi, S., Hämeri, K., Väkevä, M., and Laaksonen, A.: Adsorption of water on 8− 15 nm NaCl and $(NH_4)_2SO_4$ aerosols measured using an ultrafine tandem differential mobility analyzer, J. Phys. Chem. A, 105, 8183-8188, doi: 10.1021/jp010647l, 2001.

Schmidt, M. S., Hübner, J., and Boisen, A.: Large area fabrication of leaning silicon nanopillars for surface enhanced Raman spectroscopy, Adv. Mater., 24, OP11-OP18, doi: 10.1002/adma.201103496, 2012.

Shiraiwa, M., Kondo, Y., Moteki, N., Takegawa, N., Miyazaki, Y., and Blake, D. R.: Evolution of mixing state of black carbon in polluted air from Tokyo, Geophys. Res. Lett., 34, L16803, doi: 10.1029/2007GL029819, 2007.

Sobanska, S., Hwang, H., Choël, M., Jung, H. J., Eom, H. J., Kim, H., Barbillat, J., and Ro, C. U.: Investigation of the chemical mixing state of individual asian dust particles by the combined use of electron probe X-ray microanalysis and Raman microspectrometry, Anal. Chem., 84, 3145-3154, doi: 10.1021/ac2029584, 2012.

694 Stöckle, R. M., Suh, Y. D., Deckert, V., and Zenobi, R.: Nanoscale chemical analysis by tip-
695 enhanced Raman spectroscopy, Chem. Phys. Lett., 318, 131-136, doi: 10.1016/s0009-
696 2614(99)01451-7, 2000.
697 Sullivan, R. C., and Prather, K. A.: Recent advances in our understanding of atmospheric
698 chemistry and climate made possible by on-line aerosol analysis instrumentation, Anal.
699 Chem., 77, 3861-3886, doi: 10.1021/ac050716i, 2005.
700 Sun, L., Zhao, D., Ding, M., Xu, Z., Zhang, Z., Li, B., and Shen, D.: Controllable synthesis of
701 silver nanoparticle aggregates for surface-enhanced Raman scattering studies, J. Phys.
702 Chem. C, 115, 16295-16304, doi: 10.1021/jp205545g, 2011.
703 Sze, S.-K., Siddique, N., Sloan, J. J., and Escribano, R.: Raman spectroscopic characterization
704 of carbonaceous aerosols, Atmos. Environ., 35, 561-568, doi: 10.1016/S1352-
705 2310(00)00325-3, 2001.
706 Trainic, M., Riziq, A. A., Lavi, A., and Rudich, Y.: Role of interfacial water in the
707 heterogeneous uptake of glyoxal by mixed glycine and ammonium sulfate aerosols, J.
708 Phys. Chem. A, 116, 5948-5957, doi: 10.1021/jp2104837, 2012.
709 Uzayisenga, V., Lin, X.-D., Li, L.-M., Anema, J. R., Yang, Z.-L., Huang, Y.-F., Lin, H.-X., Li,
710 S.-B., Li, J.-F., and Tian, Z.-Q.: Synthesis, characterization, and 3D-FDTD simulation
711 of Ag@ SiO_2 nanoparticles for shell-isolated nanoparticle-enhanced Raman
712 spectroscopy, Langmuir, 28, 9140-9146, doi: 10.1021/la3005536, 2012.
713 Yang, Z., Aizpurua, J., and Xu, H.: Electromagnetic field enhancement in TERS configurations,
714 J. Raman Spectrosc., 40, 1343-1348, doi: 10.1002/jrs.2429, 2009.
715 Yeung, M. C., and Chan, C. K.: Water content and phase transitions in particles of inorganic
716 and organic species and their mixtures using micro-Raman spectroscopy, Aerosol Sci.
717 Technol., 44, 269-280, doi: 10.1080/02786820903583786, 2010.

718 Yeung, M. C., Lee, A. K. Y., and Chan, C. K.: Phase transition and hygroscopic properties of
719 internally mixed ammonium sulfate and adipic acid (AS-AA) particles by optical
720 microscopic imaging and Raman spectroscopy, Aerosol Sci. Technol., 43, 387-399,
721 doi: 10.1080/02786820802672904, 2009.
722 Zeleny, J.: On the conditions of instability of electrified drops, with applications to the
723 electrical discharge from liquid points, Proc. Cambridge Philos. Soc., 18, 71-83, 1915.
724 Zobrist, B., Marcolli, C., Pedernera, D. A., and Koop, T.: Do atmospheric aerosols form
725 glasses?, Atmos. Chem. Phys., 8, 5221-5244, doi: 10.5194/acp-8-5221-2008, 2008.
726
727
728
729
730
731
732
733
734
735
736
737
738
739
740
741
742

Table 1. Summary of intensity ratio I_{SERS}/I_{NR} at peak bands of 937, 970, 1039 and 2930 cm^{-1} for the AS, AS/SA and AS/sucrose particles and ambient PM. All Raman experiments were conducted at ambient temperature and 60% RH.

Sample	Particle size [μm]	Particle phase	Intensity ratio			
			δ(OH···O) ~937 cm^{-1}	$\nu(SO_4^{2-})$ ~970 cm^{-1}	$\nu(NO_3^-)$ ~1039 cm^{-1}	ν(C-H) ~2930 cm^{-1}
AS	31.6	Solid	NA	~ 1*	NA	NA
AS/SA	24.7	Solid	3.7	3.3	NA	2.6
AS/sucrose	23.3		NA	12.4	NA	1.6
	14.0		NA	14.8	NA	1.7
	4.0		NA	51.9	NA	6.9
	1.4	Aqueous	NA	162.0	NA	21.6
Ambient PM	<0.15	Solid	NA	1.9	1.6	NA

*No enhancement was observed at a band of $\nu(SO_4^{2-})$

Table 2. Peak position and full width at half maximum (FWHM) at the $\nu(SO_4^{2-})$ mode

Sample	Normal Raman		SERS	
	Sulfate peak [cm^{-1}]	FWHM [cm^{-1}]	Sulfate peak [cm^{-1}]	FWHM [cm^{-1}]
AS	977	7.9	977	7.5
AS/SA	977	7.4	965	20.0
AS/sucrose	980	13.5	967	16.9
Ambient PM	977	7.6	963	26.0

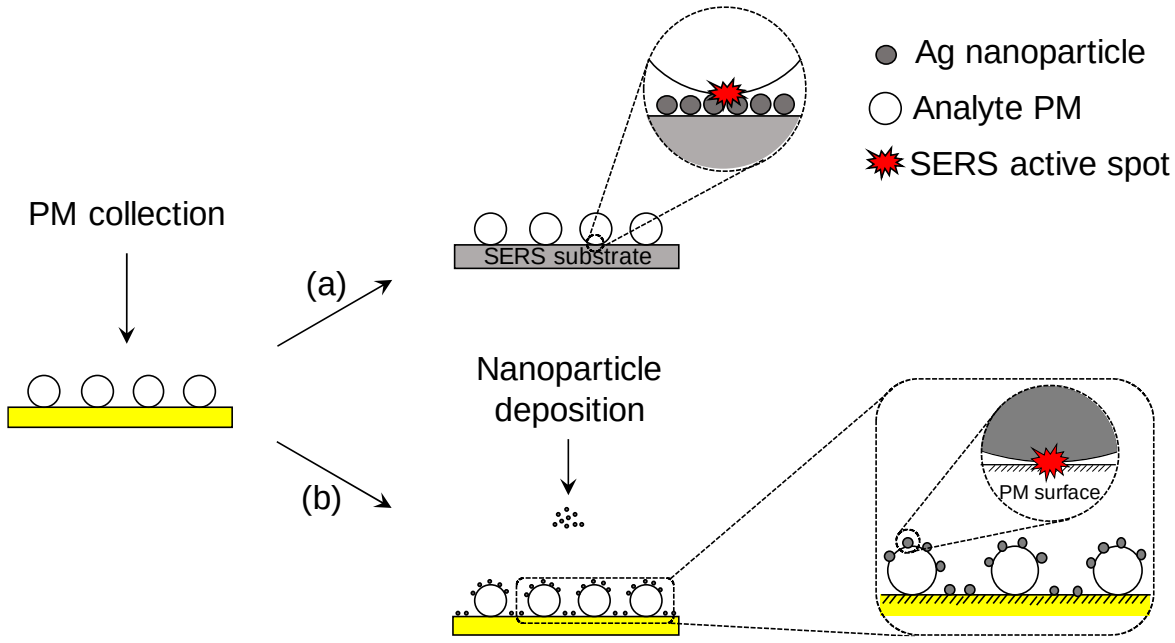

Figure 1. Schematic illustration of (a) a conventional SERS substrate approach and (b) the proposed ES-SERS approach.

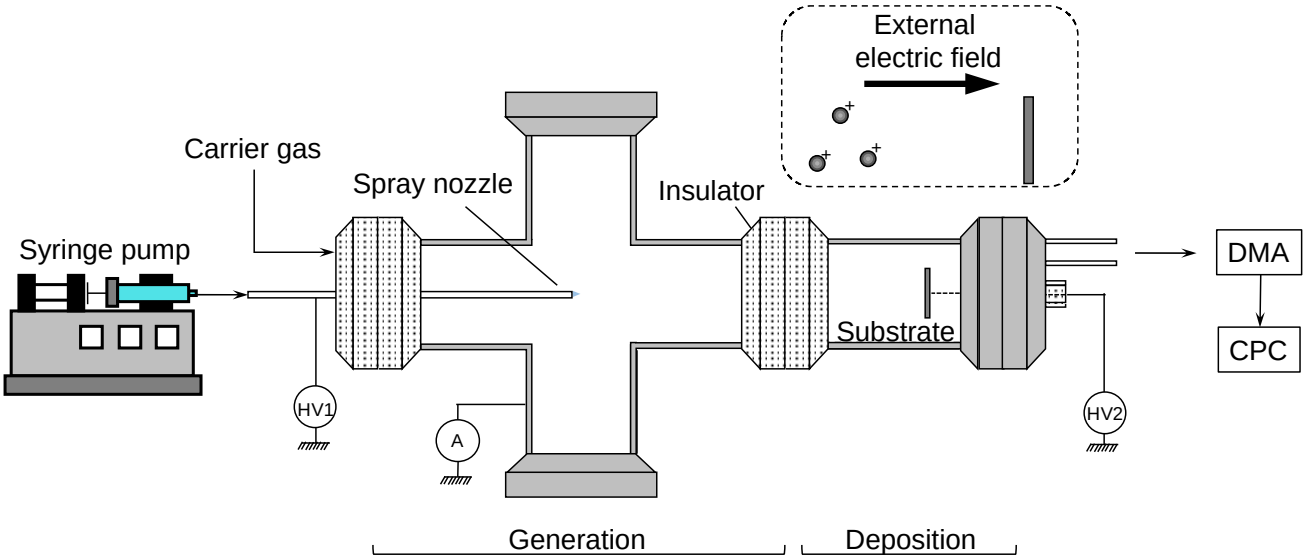

Figure 2. Schematic illustration of the electrospray system consisting of a generation and a deposition chamber.

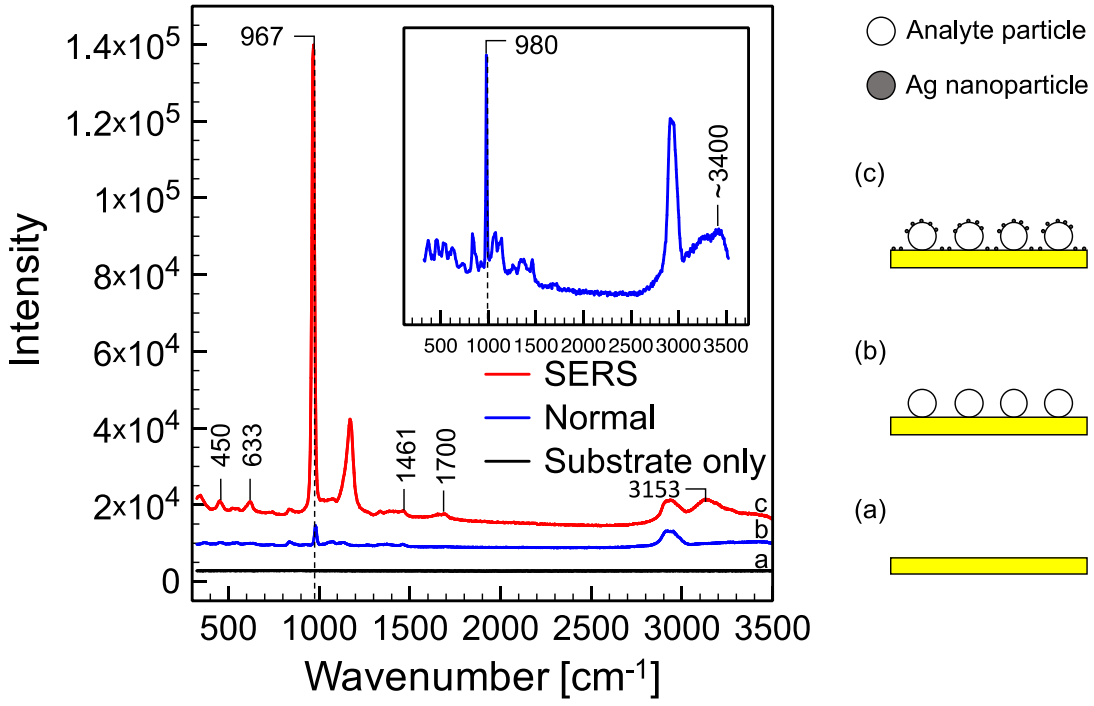

Figure 3. Normal Raman spectrum of substrate (black, a) and the AS/sucrose particles (blue, b) and SERS spectrum of the AS/sucrose particles (red, c). The inset provides a magnified view of the normal Raman spectrum for comparison. The particle sizes are 23.3 and 43.7 µm for normal Raman and SERS experiments, respectively. Schematics represent (a) substrate only, (b) analyte particles on substrate, and (c) analyte particles with Ag nanoparticles deposited on a substrate.

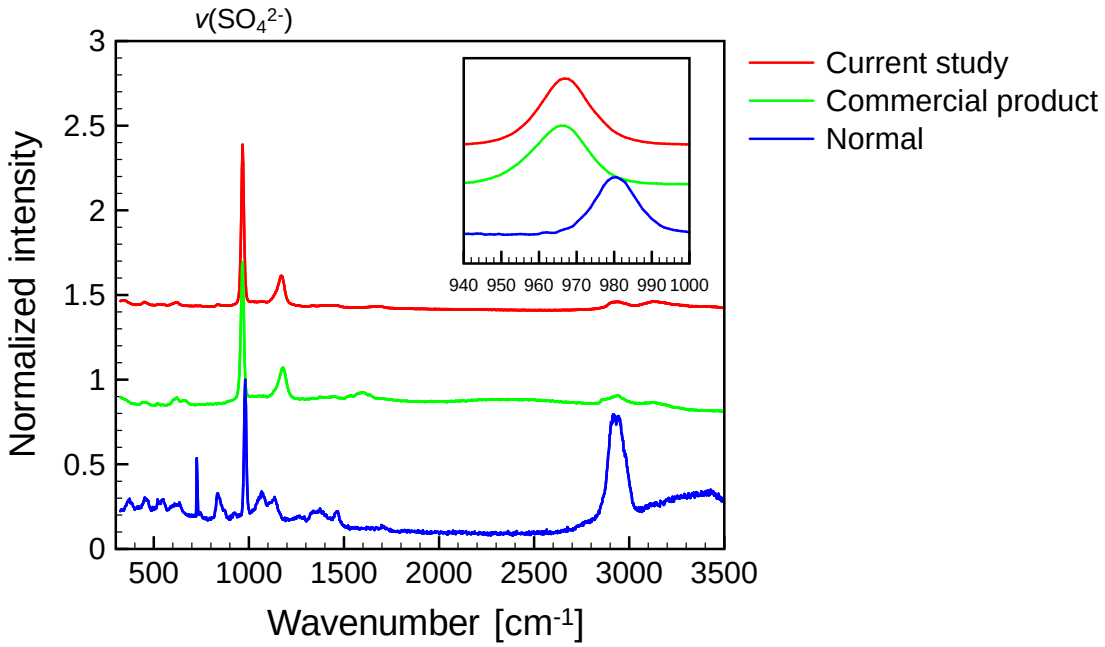

Figure 4. Normal (blue) and enhanced (green, commercial product; red, current SERS) Raman spectra of the AS/sucrose particles. Inset frame is an enlarge view of spectra at 940-1000 cm^{-1}.

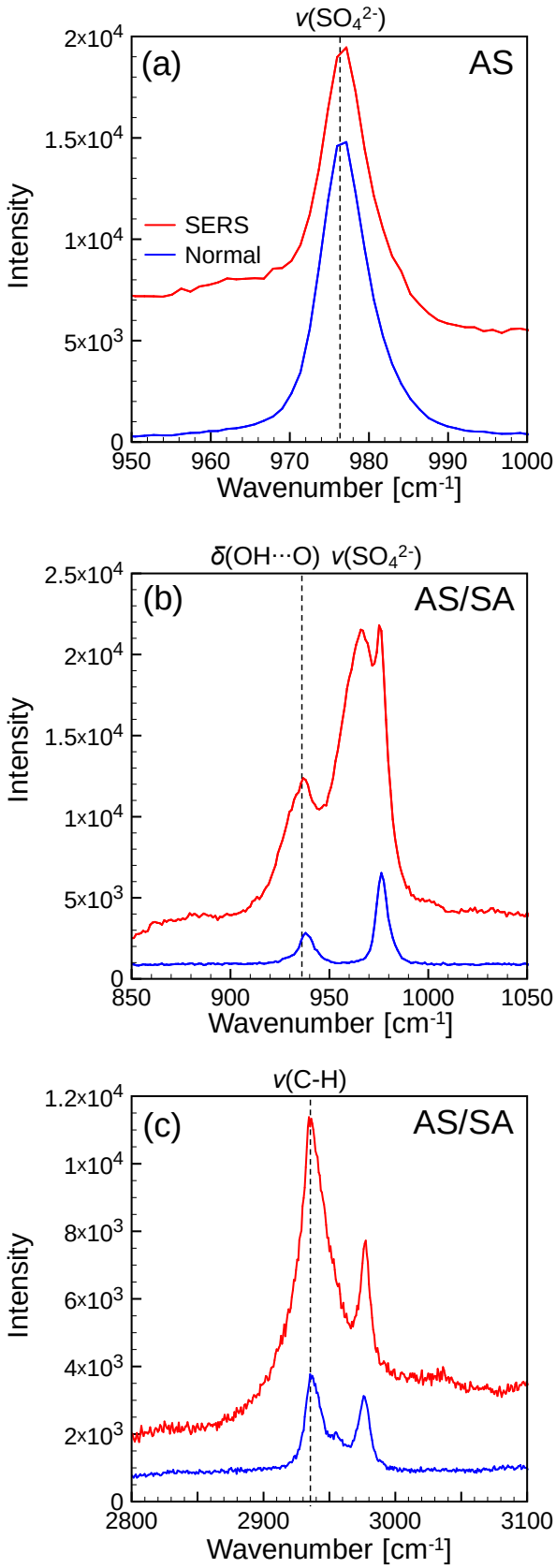

849

850 **Figure 5**. Normal and SERS spectra for (a) AS and (b) AS/SA particles at $\nu(SO_4^{2-})$ and (c)

851 ν(C-H) (only applicable to the AS/SA particles) modes.

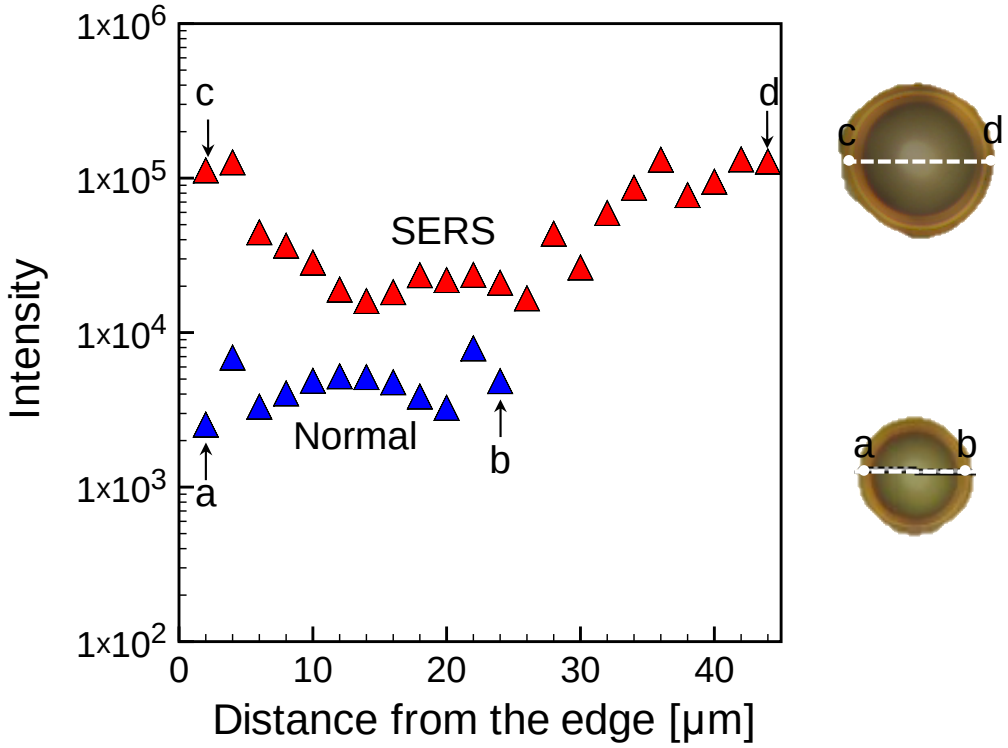

Figure 6. Raman intensity as a function of distance from edge to edge of the AS/sucrose particles: point a to b for normal Raman (blue) and point c to d for SERS (red) measurements. Optical images of corresponding particles were also shown.

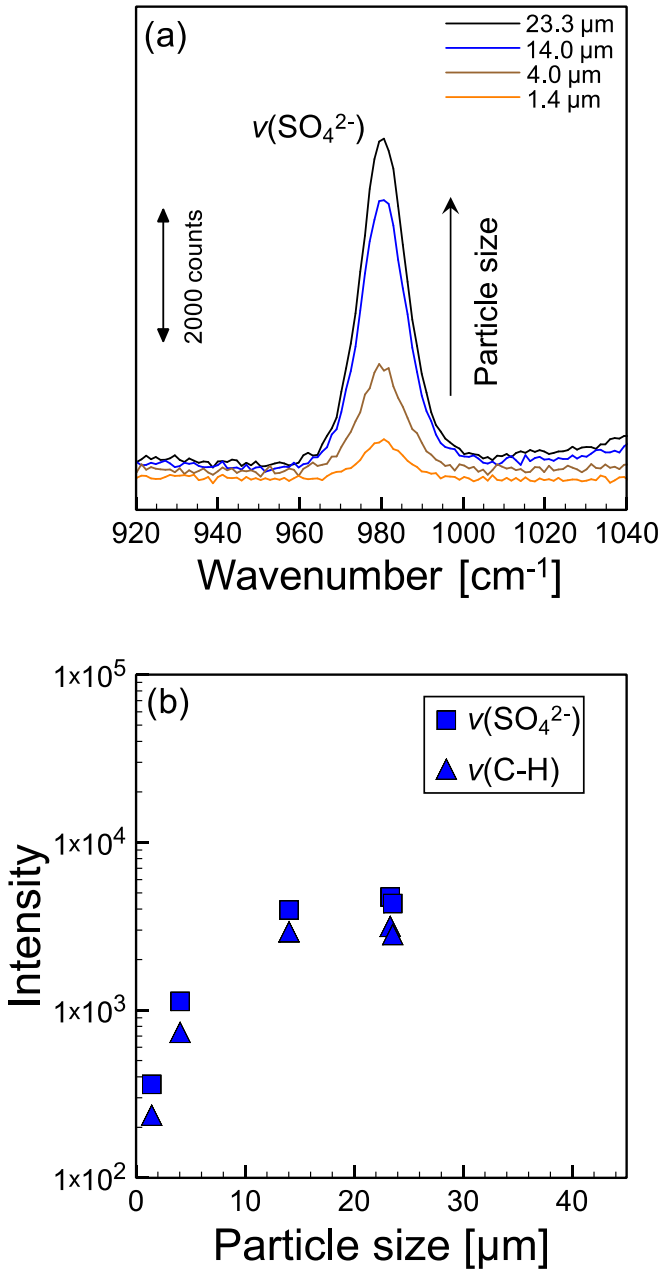

862

863 **Figure 7**. (a) Normal Raman spectra of the AS/sucrose particles as a function of particle size

864 in the lower energy region (920 ~ 1040 cm^{-1}). The peak band is assigned to the $\nu(SO_4^{2-})$

865 mode. (b) Raman intensity as a function of particle size for the $\nu(SO_4^{2-})$ and ν(C-H) modes.

866

867

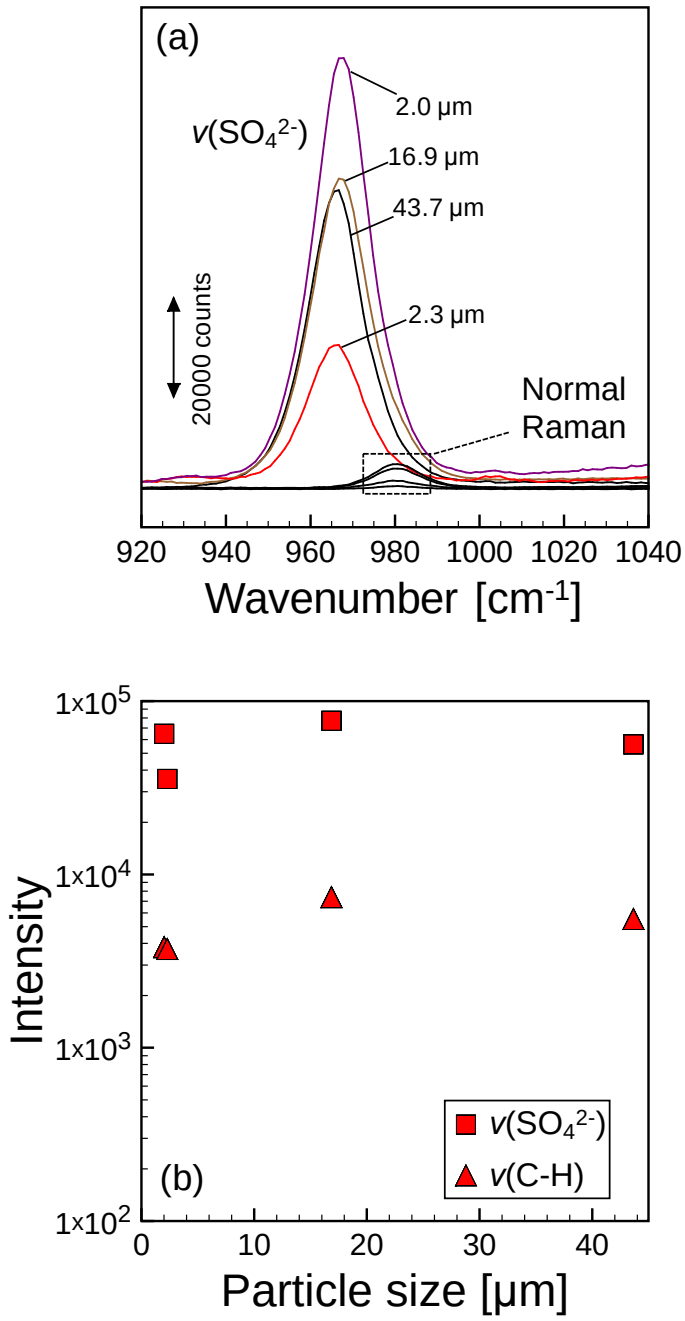

868

869 **Figure 8**. (a) Enhanced Raman spectra of the AS/sucrose particles as a function of particle

870 size in the lower energy region (920 ~ 1040 cm^{-1}). The peak band is assigned to the $\nu(SO_4^{2-})$

871 mode. The normal Raman spectra are also shown for comparison. (b) Raman intensity as a

872 function of particle size for the $\nu(SO_4^{2-})$ and ν(C-H) modes.

873

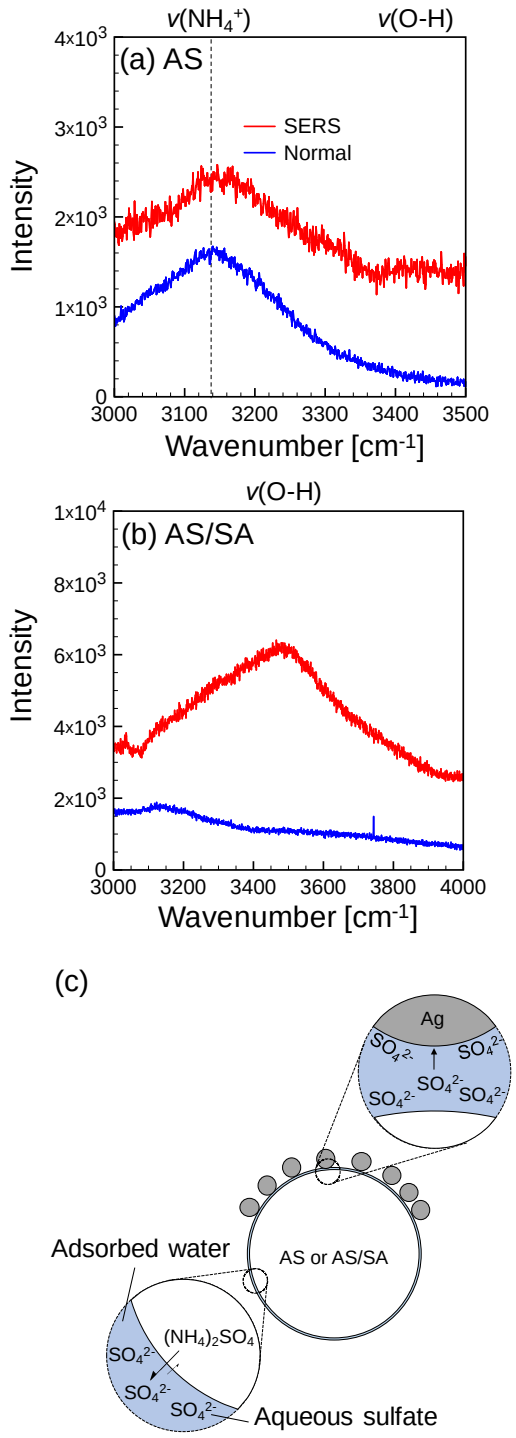

874

875 **Figure 9**. Normal (blue) and enhanced (red) Raman spectra of (a) AS and (b) AS/SA

876 particles at 3000 ~ 4000 cm^{-1}. The sizes of the AS particles are 31.6 and 30.3 μm for normal

877 Raman and SERS experiments, respectively. The sizes of the AS/SA particles are 24.7 and

878 25.5 μm for normal Raman and SERS experiments, respectively. (c) Schematic

879 representation (not to scale) of a possible role of surface-adsorbed water in facilitating

dissolution of aqueous sulfate anions that are subsequently chemisorbed on the surface of an Ag nanoparticle.

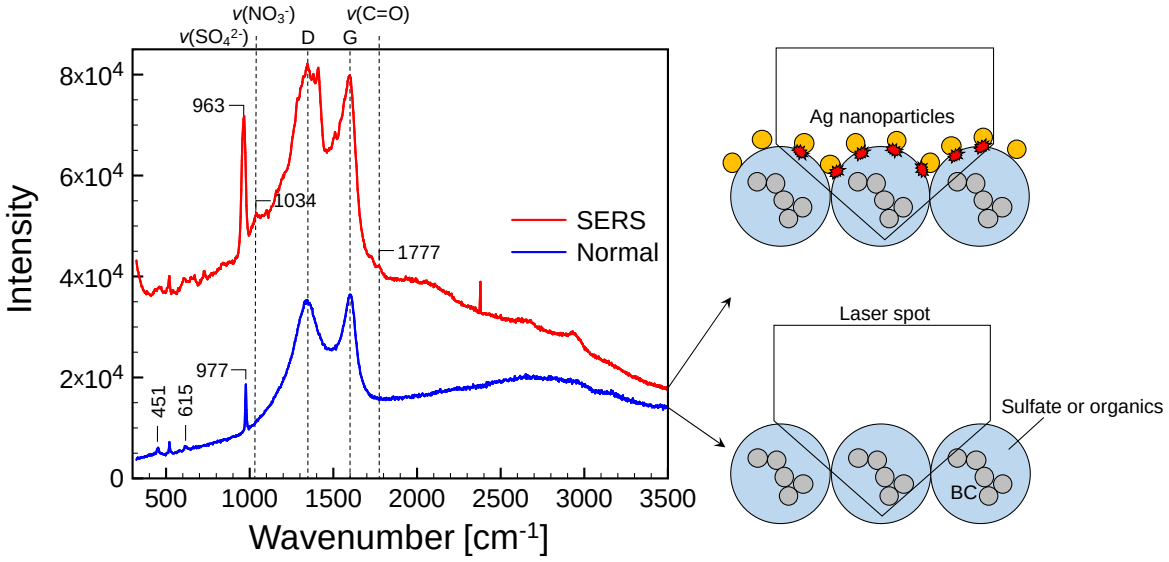

Figure 10. Normal (blue) and enhanced (red) Raman spectra of ambient PM. The particle size is between 0.05 and 0.15 μm. Sulfate peaks at 451, 615 and 977 cm^{-1}, and D and G bands at 1341 and 1598 cm^{-1}, respectively, were observed. Enhanced spectra further showed peaks at 1039 (nitrate) and 1777 (carbonyl group, indicative of organic components) cm^{-1}. The illustrations (not to scale) present experimental configurations for normal Raman and SERS measurements. The normal spectrum includes the bulk chemical compositions of BC and sulfate and the enhanced one includes the bulk compositions as well as the surface compositions (i.e. sulfate and organics).